

## RESEARCH ARTICLE

View Article Online  
View Journal | View Issue

Cite this: *Mater. Chem. Front.*,  
2020, 4, 1444

# A zinc non-halide dopant strategy enables efficient perovskite CsPbI<sub>3</sub> quantum dot-based light-emitting diodes†

Jinhang Li,<sup>a</sup> Jiawei Chen,<sup>a</sup> Leimeng Xu,<sup>a</sup> Sinan Liu,<sup>ab</sup> Si Lan,<sup>ab</sup> Xiansheng Li<sup>a</sup> and  
Jizhong Song <sup>\*acd</sup>

Metal ion doping has been considered as one of the most effective methods to achieve highly efficient perovskite light-emitting diodes (LEDs), which is significant for future high-definition displays and high-quality lighting. However, its exact function is still uncertain because the doping of metal ions is also accompanied by the introduction of halide ions and halide-rich circumstances, which can enhance the optoelectronic properties as well. In this work, a zinc non-halide dopant strategy was employed to specifically study the effect of Zn<sup>2+</sup> on CsPbI<sub>3</sub> quantum dots (QDs). We confirmed that Zn<sup>2+</sup> was doped into the perovskites interstitially via X-ray diffraction (XRD) and pair distribution function (PDF) analysis. Zn<sup>2+</sup>-doped CsPbI<sub>3</sub> QDs exhibited higher emission properties with 120% enhancement in the photoluminescence quantum yield (PLQY) compared with pristine CsPbI<sub>3</sub> QDs. The Zn<sup>2+</sup>-doped CsPbI<sub>3</sub> QD-based LEDs (QLEDs) showed nearly two-fold increase in the external quantum efficiency (EQE) versus the control device, and it improved from 7.5% to 14.6%. Besides, a maximum current efficiency of 0.83 cd A<sup>-1</sup> and the highest luminance of 378 cd m<sup>-2</sup> were achieved. These results certify that Zn<sup>2+</sup> doping enables high-performance QLEDs without the introduction of halide ions, which is beneficial for the further research on doped perovskite fields and lays the foundation for the future practical applications of QLEDs.

Received 4th December 2019,  
Accepted 27th February 2020

DOI: 10.1039/c9qm00734b

rsc.li/frontiers-materials

## Introduction

Perovskite quantum dots (QDs) with superior properties, including high photoluminescence quantum yield (PLQY), narrow full width at half maximum (FWHM) and finely tunable emission spectra in the visible region, have attracted significant attention in next-generation high-definition displays and high-quality lighting.<sup>1–3</sup> On the basis of these excellent properties, a large number of studies have been carried out to improve the external quantum efficiency (EQE) of perovskite QD-based light-emitting diodes (QLEDs) to enable efficient light emission with less energy consumption.<sup>4–6</sup> During the past few years, there has been impressive progress in the EQE of perovskite

LEDs. Up to now, the EQE values of perovskite QLEDs have been reported to be 16.48%,<sup>7</sup> 21.3%,<sup>8</sup> and 2.12%<sup>9</sup> for green, red, and blue QLEDs, respectively.

These high EQE values and other distinguished properties of QLEDs can be realized by different methods: doping,<sup>10,11</sup> surface ligand engineering,<sup>12–14</sup> defect passivation,<sup>15,16</sup> optimization of the device architecture,<sup>17,18</sup> etc.<sup>19–21</sup> Among these methods, doping is commonly and frequently used to boost efficiencies. In traditional Cd-based QDs, transition metal-doped QDs have come up as a new class of light-emitting materials that can retain all the advantages of undoped QDs and also overcome some of the intrinsic disadvantages such as self-absorption and sensitivity to thermal, chemical, and photochemical disturbances compared to their undoped counterparts.<sup>22,23</sup> In 2009, Stouwdam *et al.*<sup>24</sup> reported efficient LEDs based on Cu-doped CdS QDs with an increased EQE of 5%. Later, Santra's group<sup>25</sup> employed Mn doping to boost the EQE of CdS-based QLEDs up to 5.4%.

In perovskite QDs, doping is also a frequently used method. With the structure of perovskites being ABX<sub>3</sub> (A is normally Cs<sup>+</sup>, formamidinium (FA) cation, methylamine (MA) cation and other organic molecules; B represents metal ions such as Pb<sup>2+</sup>; X represents halide ions like Cl<sup>-</sup>, Br<sup>-</sup>, and I<sup>-</sup>),<sup>26,27</sup> divalent metal ion doping has been considered as an effective method to

<sup>a</sup> School of Materials Science and Engineering, Nanjing University of Science and Technology, Nanjing 210094, China. E-mail: songjizhong@njust.edu.cn

<sup>b</sup> Herbert Gleiter Institute of Nanoscience, Nanjing University of Science and Technology, Nanjing 210094, China

<sup>c</sup> MIT Key Laboratory of Advanced Display Materials and Devices, Institute of Optoelectronics & Nanomaterials, Nanjing University of Science and Technology, Nanjing 210094, China

<sup>d</sup> School of Physics and Microelectronics, Zhengzhou University, Zhengzhou 450001, China

† Electronic supplementary information (ESI) available. See DOI: 10.1039/c9qm00734b

enhance EQE because of the effect on reducing non-radiative recombination, lowering charge injection barriers, and enhancing carrier transport properties.<sup>28–30</sup> In 2018, Rogach's group reported that strontium doping and chlorine passivation enhanced the EQE of CsPbI<sub>3</sub> QDs to 13.5%.<sup>31</sup> Recently, through the employment of Zn<sup>2+</sup>, their group further improved the EQE of CsPbI<sub>3</sub> QDs to 15.1%.<sup>32</sup> The introduction of Zn<sup>2+</sup> eliminates defects to some degree, which was validated by the improved radiative decay rates by 4.1-fold and increased PLQY values from 61.3% to 98.5%. Besides, many other papers have reported similar results that the doping of metal ions can improve the properties of perovskites.<sup>33–35</sup>

However, a divalent dopant element is introduced in the form of MX<sub>2</sub> (M = metal; X = Cl, Br, I and other halides).<sup>36,37</sup> Thus, halide ions are also introduced during divalent doping. Recently, researchers have presented that under halide-rich growth conditions, better emission properties and higher quality LEDs can be achieved.<sup>38,39</sup> For example, Liu *et al.*<sup>40</sup> found that under halide-rich circumstances, CsPbBr<sub>3</sub> QDs with a Pb/Br ratio of 1:4 show higher PLQYs and improved maximal luminance of 12 090 cd m<sup>-2</sup> compared with that in regular circumstances. Kye *et al.* also demonstrated that I<sup>-</sup>-rich growth conditions could control the formation of the cation vacancies of CsPbI<sub>3</sub> QDs and enhance the quality of QDs.<sup>39</sup> In addition, Dong's group reported that a synthetic approach involving a high Br/Pb ratio could achieve narrower photoluminescence by a high level of size control and ensemble uniformity.<sup>38</sup> Therefore, how M<sup>2+</sup> really affects perovskite QDs and enhances the luminescence properties without the existence of X<sup>-</sup> become meaningful problems that need to be addressed, and this is of great significance for the future development of highly efficient QLEDs.

Besides, CsPbI<sub>3</sub> perovskite QDs with deep-red emission (650–700 nm) have great potential in the next-generation high-definition displays and solid-state lighting, particularly for the specific demands of high visibility and applications like horticultural lighting, because deep-red light has better visibility than red light and the chlorophyll would have the most active synthesis under deep red luminescence.<sup>41</sup> In addition, deep red light is promising in the construction of warm white light-emitting diodes in solid-state lighting applications, and numerous works about iodide-based perovskites have been extensively studied.<sup>42–46</sup>

In this paper, we developed a zinc non-halide dopant strategy to clarify the internal mechanism of Zn<sup>2+</sup> doping, figure out its impact on the structure and properties of CsPbI<sub>3</sub> perovskite QDs, and construct high-performance QLEDs. Zn<sup>2+</sup> ions were doped in the interstitial sites and caused QD lattice expansion, as validated through X-ray diffraction (XRD) and pair distribution function (PDF). Besides, the Zn<sup>2+</sup>-doped CsPbI<sub>3</sub> perovskite QDs exhibited an improved PLQY of 76%, increased photoluminescence (PL) lifetime and lower trap density, which suggested less defect sites and more effective exciton recombination in the doped QDs. Hence, an EQE up to 14.6% for perovskite QLEDs was achieved through the proposed zinc non-halide dopant strategy. In addition to the use of zinc acetylacetonate (ZnAcAc) as the dopant that improved the EQE of QLEDs, it was proved that other zinc non-halide salts, including zinc acetate (ZnAc) and zinc stearate (ZnSt),

were feasible for improving the performance of QLEDs. This result demonstrates the universality of the zinc non-halide dopant strategy and its potential in future practical applications.

## Results and discussion

Zinc-doped CsPbI<sub>3</sub> QDs were synthesized by the common hot injection method,<sup>47</sup> in which different Zn<sup>2+</sup> salts were added to the PbI<sub>2</sub> precursor as the zinc source (Fig. 1a); the detailed synthetic conditions have been listed in the Experimental section. To rule out the effect of halide ions and demonstrate the universality of the zinc non-halide dopant strategy, Zn<sup>2+</sup> salts with different negative ions including Ac<sup>-</sup>, AcAc<sup>-</sup> and St<sup>-</sup>, the structures of which are shown in the right part of Fig. 1a, were doped into CsPbI<sub>3</sub> perovskite QDs.

Our proposed zinc non-halide dopant strategy could effectively decrease the defect sites and non-radiative recombination, resulting in higher emission properties (Fig. 1b and c). After the doping of all the Zn<sup>2+</sup> salts mentioned above, the perovskite QDs displayed higher emission properties. The Zn<sup>2+</sup>-doped solution emitted stronger red light *versus* the undoped QD solution, as shown in the inset of Fig. 1d. Accordingly, as shown in the steady-state PL spectra achieved under the same ultra-violet light excitation (Fig. 1d), the PL intensity of Zn<sup>2+</sup>-doped CsPbI<sub>3</sub> QDs is enhanced, which indicates the increased electron-hole radiative recombination. After doping, the peak slightly shifts from 684 nm to 682 nm, which might be attributed to the increased band energy with the introduction of Zn<sup>2+</sup>.<sup>32</sup> Besides, the corresponding doped QDs exhibited more outstanding luminescence properties with the PLQY increasing to as high as 76%, as validated by the absolute PLQY measurements (Fig. 1e), compared with the undoped one.

The effect of Zn<sup>2+</sup> on the crystal structure of CsPbI<sub>3</sub> QDs was first investigated by XRD to reveal the doping mechanism of Zn<sup>2+</sup> without the introduction of halide ions. As shown in Fig. 2a, the main diffraction peaks are located at 14.1°, 20.0° and 28.6°, corresponding to the (100), (110) and (200) planes of the cubic perovskite structure.<sup>48</sup> After doping Zn<sup>2+</sup>, no new diffraction peaks appear and the existing peaks are slightly enhanced, indicating that the crystalline phase does not change and the crystallinity increases. After doping, the diffraction peak shifts to a smaller angle for all the Zn<sup>2+</sup> salts with different negative ions (Fig. 2b). The peak shift towards smaller angles signified lattice expansion, which might result from the Zn<sup>2+</sup> ions residing in the interstitial sites. Because the ionic radius of Zn<sup>2+</sup> (74 pm) is smaller than that of Pb<sup>2+</sup> (119 pm), the doping of Zn<sup>2+</sup> into the crystal lattice of CsPbI<sub>3</sub> QDs through interstitial doping would be easy.

Transmission electron microscopy (TEM) showed that the average diameter increased from 12.80 ± 0.3 nm up to 15.50 ± 0.2 nm (Fig. 2c and d). The relevant TEM images and lognormal distribution histograms of pristine and doped CsPbI<sub>3</sub> QDs by using different Zn salts are provided in Fig. S1 (ESI†). In agreement with the lattice expansion observed from the XRD results, the interplanar distance was enlarged from 6.1 Å to 6.3 Å

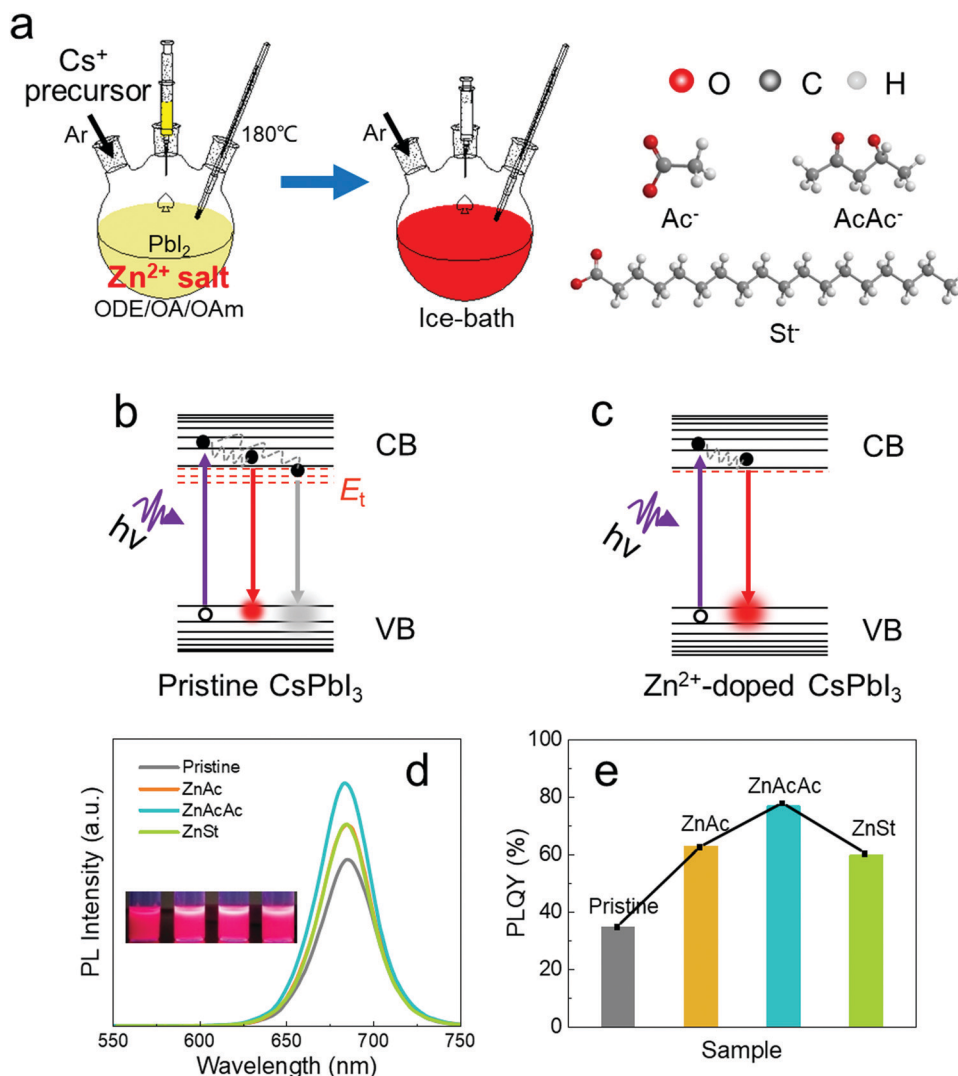


**Fig. 1** (a) Left: The synthetic diagram of CsPbI<sub>3</sub> QDs by hot injection method; right: the corresponding structure of employed different negative ions of Zn<sup>2+</sup> salts. (b and c) Schematics of radiative and non-radiative recombination of QDs and defect sites before and after Zn<sup>2+</sup> doping. (d) The PL spectra of pristine and Zn<sup>2+</sup>-doped CsPbI<sub>3</sub> QDs and their photograph under UV lamps. (e) The PLQY spectra of pristine and Zn<sup>2+</sup>-doped CsPbI<sub>3</sub> QDs.

(insets of Fig. 2c, d and Fig. S2, ESI†). Although doping Zn<sup>2+</sup> resulted in crystal structure expansion, the film roughness showed no obvious degradation, as presented by atomic force microscopy (AFM) (Fig. S3 and S4, ESI†).

Taking the zinc source introduced in the form of ZnAcAc as an example, energy dispersive X-ray spectroscopy (EDS) chemical mapping was performed to further confirm the incorporation of Zn<sup>2+</sup>. It is shown from the EDS results (Fig. 2e–h) that the Zn element is incorporated in CsPbI<sub>3</sub> QDs, which is in accordance with previous reports.<sup>32</sup> Meanwhile, as shown in the X-ray photoelectron spectroscopy (XPS) results (Fig. S5, ESI†), QDs synthesized with Zn<sup>2+</sup> exhibited a new peak located at 1044.6 eV, which could be assigned to the 2p signals of Zn<sup>2+</sup> and further proved that the Zn<sup>2+</sup> ions were incorporated.

Although the whole lattice showed an expansion trend, as validated by the XRD and TEM results, it was still uncertain whether the Zn<sup>2+</sup> ions were doped as interstitial ions. The perovskite structure is flexible, *i.e.*, it can tolerate different types of cations

on the A- and B-sites as long as the charge neutrality is maintained.<sup>49,50</sup> The XRD method, mainly used for long range structure characterizations, cannot provide detailed local structure information, which is important for the optoelectronic properties of perovskites.<sup>51</sup> Therefore, we employed PDF to explore the local structure information and confirm the evolution of the CsPbI<sub>3</sub> QD structure after doping. Fig. 3a exhibits the characterized instrument schematic of PDF. With the high-energy X-ray beam focused on the CsPbI<sub>3</sub> QD sample, two-dimensional diffraction signals can be received, collected and converted to three-dimensional PDF information ( $G(r)$ , where  $r$  is the atomic pair distance) by Fourier transforming  $S(Q)$ :

$$G(r) = 4\pi r(\rho(r) - \rho_0) = \frac{2}{\pi} \int_0^\infty Q(S(Q) - 1) \sin(Qr) dQ$$

Here,  $\rho(r)$  is the atomic pair density function,  $\rho_0$  is the number density of atoms in the material,  $Q$  is the magnitude of the

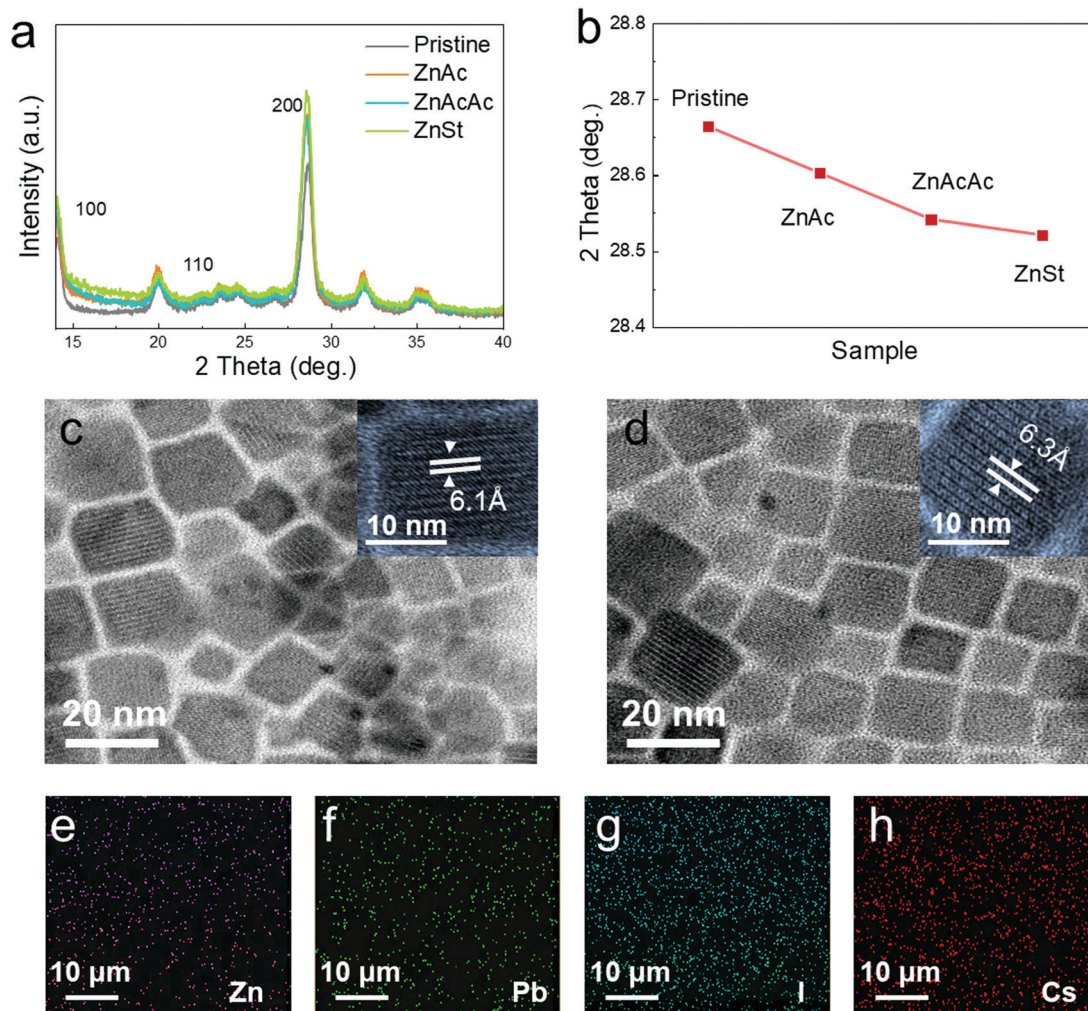


**Fig. 2** (a and b) XRD patterns of pristine CsPbI<sub>3</sub> QDs and Zn<sup>2+</sup>-doped QDs, and the local enlarged (200) peak. (c and d) TEM images of the (left) pristine and (right) Zn<sup>2+</sup>-doped CsPbI<sub>3</sub> QDs with their corresponding enlarged TEM images as insets. (e–h) Element mapping of Zn<sup>2+</sup>-doped CsPbI<sub>3</sub> QDs, corresponding to Zn, Cs, Pb, and I.

scattering vector (or momentum transfer), and  $r$  is the interatomic (atom–atom) distance.

As mentioned in a related paper, the main peaks of the CsPbI<sub>3</sub> pair distribution are located at 3.2 Å, 4.6 Å and 6.4 Å, corresponding to the Pb–I bond, Cs–Oct (octahedron) bond/I–I bond and Oct–Oct bond/Pb–Pb bond.<sup>52</sup> As shown in Fig. 3b, no peaks corresponding to the Zn–I bond (2.94 Å) appear after Zn<sup>2+</sup> doping, which means that the Zn<sup>2+</sup> ions have not taken the place of Pb<sup>2+</sup> ions and formed Zn–I octahedra. However, there were apparent movements and changes in the Cs–Oct bond. In order to separate the peaks of near bonds from the main PDF peak, we converted  $G(r)$  into  $T(r)$ :

$$T(r) = 4\pi r \rho(r) = 4\pi \rho_0 r + G(r)$$

Here, the atomic pair distributions follow Gaussian profiles (Fig. S6, ESI†) and can fit different peaks. We conducted Gaussian fitting towards the peak of the Cs–Oct bond before (Fig. 3c) and after doping (Fig. 3d). The results showed that a peak located at 4.35 Å appeared. Because of the small radius

of Zn<sup>2+</sup>, we attributed the appeared peak and the left shift in the Cs–Oct peak to the doping of Zn<sup>2+</sup> as interstitial ions between the octahedral structure. Based on the XRD and PDF analyses, a schematic of Zn<sup>2+</sup> doped in interstitial sites and lattice expansion is shown in Fig. S7 (ESI†).

Generally, the crystal structure of a material is related to its bandgap. To further evaluate the optical properties after the structural changes resulting from Zn<sup>2+</sup> doping, the absorption spectra of pristine and Zn<sup>2+</sup>-doped CsPbI<sub>3</sub> QDs were measured. The band tails of CsPbI<sub>3</sub> QDs with or without doping in the absorption data show changes in the Urbach energy ( $E_u$ ). The  $E_u$  values of these materials are calculated from the formula mentioned below:

$$E_u = \frac{E}{\ln \frac{\alpha}{\alpha_0}}$$

Here,  $\alpha_0$  is a constant.<sup>53,54</sup> According to the formula,  $E_u$  can be obtained as the reciprocal of the slope near the band edge, as shown in Fig. 4a and Fig. S8 (ESI†). Because the Urbach energy represents the tail of the localized states in the bandgap,<sup>55</sup>  $E_u$  is

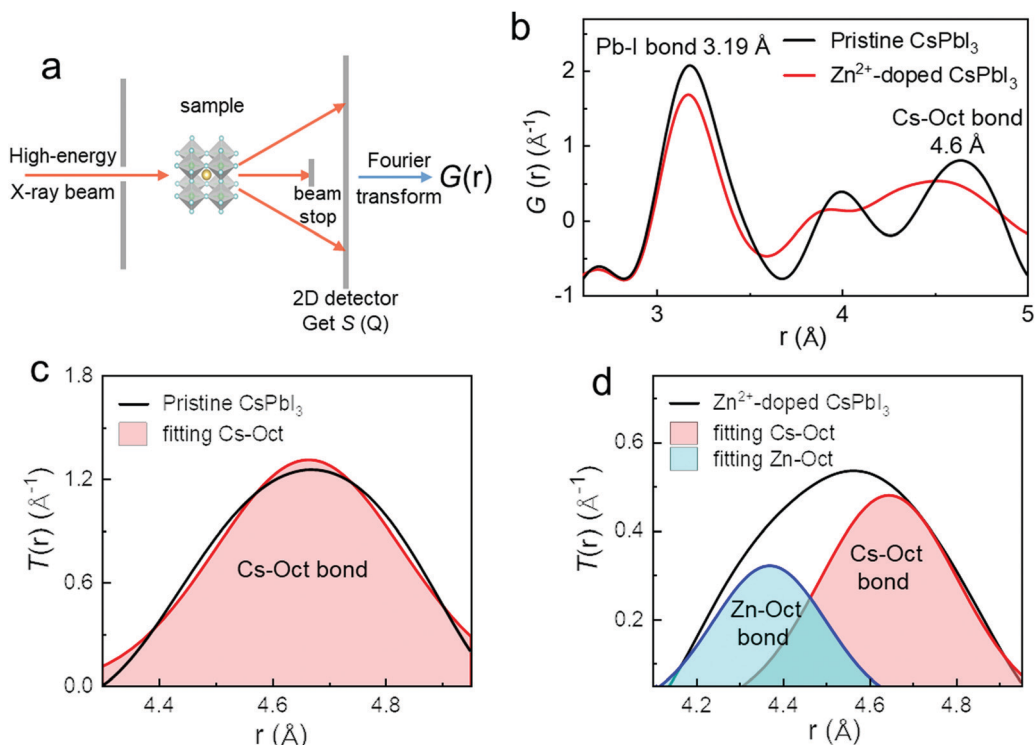


Fig. 3 (a) Schematic of high-energy diffraction instrument set-up. (b) The pair distribution function  $G(r)$  of pristine  $\text{CsPbI}_3$  QDs and  $\text{Zn}^{2+}$ -doped QDs, respectively. (c and d) The Gaussian fitting of partial peak (Cs–Oct bond) to synchrotron X-ray PDF  $T(r)$  before and after  $\text{Zn}^{2+}$  doping.

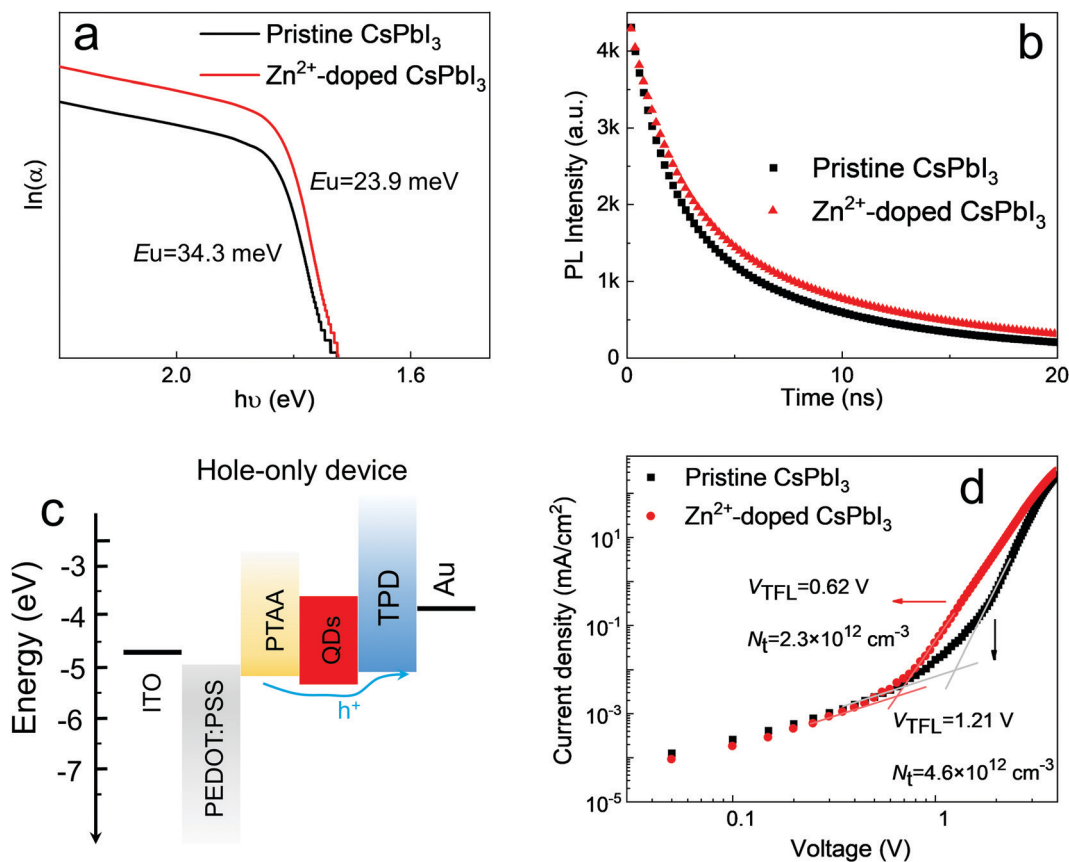


Fig. 4 (a) Relationship of  $\ln(\alpha)$  versus energy for the calculation of Urbach energy of pristine  $\text{CsPbI}_3$  and  $\text{Zn}^{2+}$ -doped  $\text{CsPbI}_3$  QDs. (b) PL decay curves of pristine  $\text{CsPbI}_3$  and  $\text{Zn}^{2+}$ -doped  $\text{CsPbI}_3$  QDs. (c) Device energy-level diagrams of hole-only devices. (d) Current–voltage characteristics of hole-only device.

reduced from 34.3 eV to 23.9 eV, suggesting that the density of the localized states near the bandgap decreases after  $\text{Zn}^{2+}$  doping.

Fig. 4b shows the PL decay curves obtained from pristine and doped QDs. The average lifetime of the pristine film was about 7.22 ns, which increased to 11.76 ns for  $\text{Zn}^{2+}$ -doped QDs; the detailed information is shown in Table S1 (ESI†). Longer PL decay times manifest more effective radiative recombination pathways, which can suggest fewer defect centers, and this is favorable to reduce the trapping of excitons and increase the radiative recombination.

Attempting to further verify the difference in trap sites and densities, space-charge-limited current (SCLC) measurements were operated. A “hole-only” device with a structure of indium tin oxide (ITO)/poly(3,4-ethylenedioxythiophene):poly(styrenesulfonate) (PEDOT:PSS)/poly(bis(4-phenyl)(2,4,6-trimethylphenyl)amine) (PTAA)/QDs/poly[ $N,N'$ -bis(4-butylphenyl)- $N,N'$ -bis(phenyl)-benzidine] (TPD)/Au was fabricated (Fig. 4c). Under low applied voltages, the  $I$ - $V$  relationship of the current density with the bias voltage was found to be linear and ohmic, indicating an ideal interface capable of injecting enough charges from the electrodes into the semiconducting materials to sustain the SCLC transport with negligible trap states. On increasing the bias voltage, the trap states were observed to be gradually filled by holes until the device reached the trap-filled limit (TFL) stage.<sup>56,57</sup>

$$V_{\text{TFL}} = \frac{en_t L^2}{2\epsilon\epsilon_0}$$

Here,  $n_t$  is the trap-state density,  $L$  is the layer thickness,  $\epsilon$  is the relative dielectric constant and  $\epsilon_0$  the vacuum permittivity. The  $V_{\text{TFL}}$  values can be used to reflect the transition from the ohmic stage to the TFL stage, and the density of trap states ( $n_t$ ) is proportional to  $V_{\text{TFL}}$ . From the SCLC data (Fig. 4d and Fig. S9, ESI†), the  $V_{\text{TFL}}$  values with and without  $\text{Zn}^{2+}$  doping were 0.62 V and 1.21 V, respectively. Hence, the obtained  $n_t$  calculated from the  $V_{\text{TFL}}$  value for the  $\text{Zn}^{2+}$ -doped  $\text{CsPbI}_3$  QD film was estimated to be  $2.3 \times 10^{12} \text{ cm}^{-3}$ , which was lower than that for the pure  $\text{CsPbI}_3$  QD film ( $4.6 \times 10^{12} \text{ cm}^{-3}$ ). The SCLC measurements demonstrated lower trap density and less defect sites of  $\text{Zn}^{2+}$ -doped  $\text{CsPbI}_3$ , which were in accordance with the results of PLQY and PL decay; this is extremely desired for constructing high-performance LEDs.

The robustness of the higher emission properties and lower trap density of the QD films is expected to provide high exciton recombination efficiency in devices. The device performances of QLEDs are presented in Fig. 5. The device (Fig. 5a) is made up of multiple layers in the following order: ITO, PEDOT:PSS, PTAA, perovskite QDs, 1,3,5-tris(1-phenyl-1H-benzimidazol-2-yl)-benzene (TPBi, 40 nm), and LiF/Au (1/100 nm). The corresponding device energy-level diagrams are shown in Fig. S10 (ESI†).

The typical electroluminescence (EL) spectrum of the device containing  $\text{CsPbI}_3$  and  $\text{Zn}^{2+}$ -doped  $\text{CsPbI}_3$  QDs consists of peaks located at 689 nm, and 687 nm, showing a similar shift to that of the PL peak (Fig. 5b). The Commission Internationale de l'Eclairage (CIE) chromaticity coordinates of  $\text{CsPbI}_3$  and

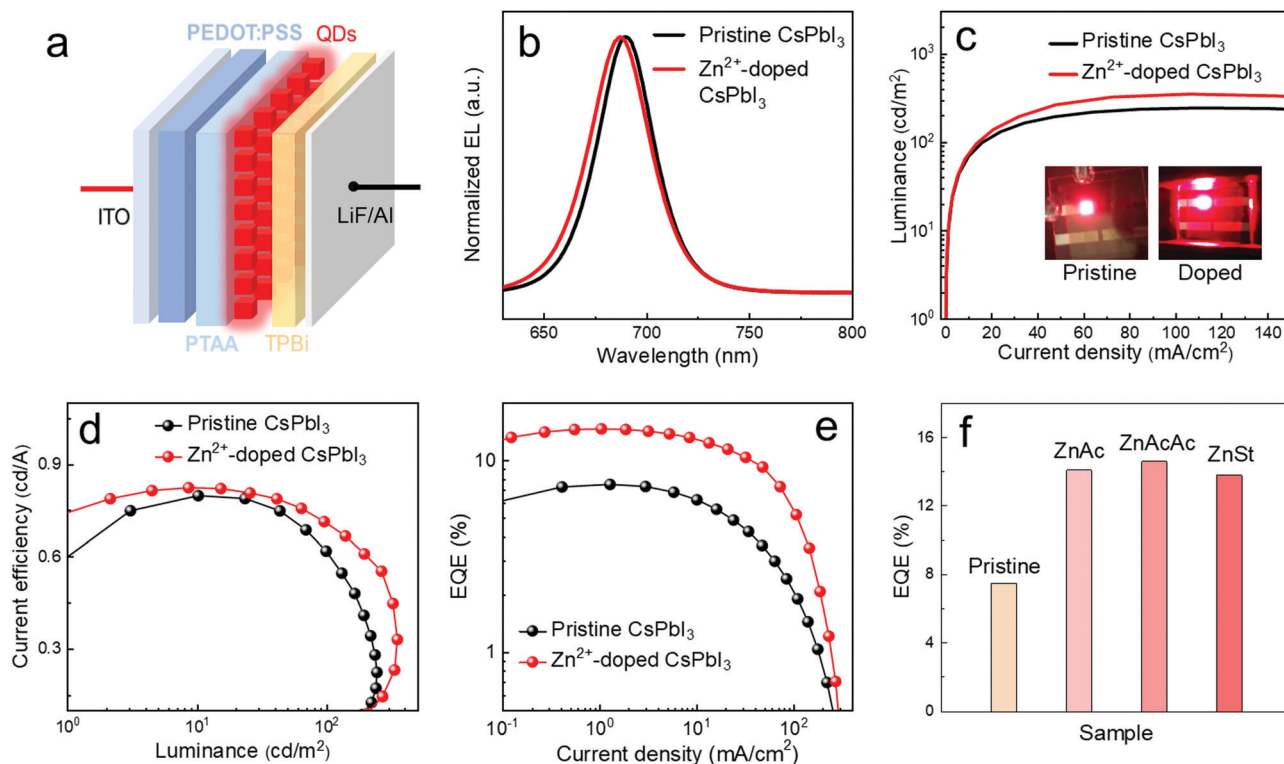


**Fig. 5** (a) Schematic illustration of multilayer perovskite QLED device. (b) Normalized EL spectra at an applied voltage of 5 V before and after  $\text{Zn}^{2+}$  doping. (c) The luminance–current density characteristics of QLEDs; inset shows photographs of the two devices. (d) Current efficiency of the devices as a function of luminance. (e) EQE of the devices as a function of current density. (f) EQE values for doping with different  $\text{Zn}^{2+}$  salts.

Zn<sup>2+</sup>-doped CsPbI<sub>3</sub> QD films are (0.72, 0.27) and (0.72, 0.28), showing nearly no difference (Fig. S11, ESI†).

The luminance–current density curve of the devices (Fig. 5c) was measured and it was found that the devices with Zn<sup>2+</sup> ions showed higher luminance under the same current density. The luminance after Zn<sup>2+</sup> doping improved from 221 cd m<sup>−2</sup> to 378 cd m<sup>−2</sup>, which validated the enhanced exciton recombination in Zn<sup>2+</sup>-doped CsPbI<sub>3</sub> QDs. Also, luminance and current density are the key factors of current efficiency, which is directly proportional to luminance and inversely proportional to current density. Therefore, the higher luminance under the same current density of Zn<sup>2+</sup>-doped CsPbI<sub>3</sub> QDs resulted in higher current efficiency than that for pristine CsPbI<sub>3</sub> QDs (Fig. 5d), which increased from 0.75 cd A<sup>−1</sup> to 0.83 cd A<sup>−1</sup>.

Based on the enhanced exciton recombination, the devices containing Zn<sup>2+</sup>-doped CsPbI<sub>3</sub> QDs demonstrated higher EQE; the peak EQE reached as high as 14.6%, as shown in Fig. 5e, which was higher than that of the pristine one (7.5%) and achieved nearly 100% increase. Similar results were also obtained for other Zn salts (Fig. 5f and Fig. S12, S13, ESI†). The increase in EQE indicates that Zn<sup>2+</sup> doping can effectively enhance the radiative recombination, which is in accordance with the characterization results mentioned above. The achieved 14.6% EQE is in the forefront for reported CsPbI<sub>3</sub> QLEDs. The EQE progress of CsPbI<sub>3</sub> QLEDs and detailed information are provided in Fig. S14 and Table S2 (ESI†).

## Conclusions

In conclusion, we investigated the effects of Zn<sup>2+</sup> on CsPbI<sub>3</sub> perovskite QDs through different zinc non-halide dopants. It was observed that Zn<sup>2+</sup> was doped into CsPbI<sub>3</sub> QDs in an interstitial position, as elucidated by the PDF and XRD methods. Resulting from higher PLQY, lower trap density, and more effective exciton recombination after doping, high-performance perovskite QLEDs were achieved. The EQE of the device increased from 7.5% to 14.6%, which was nearly 2-fold increase *versus* that for the device based on undoped CsPbI<sub>3</sub> QDs. These findings would help us achieve a better understanding of the effect of doping metal ions, especially divalent ions, on the structure and properties of perovskite materials and devices, which is of great value for the further development of perovskite optoelectronic devices.

## Experimental section

### Materials

PbI<sub>2</sub> (from Aladdin, 99.99%), cesium stearate (CsSt, 98% pure, from J&K), ZnAc (from Macklin, 99.99%), ZnAcAc (from Macklin, 98%), ZnSt (from Macklin, 98%), oleic acid (OA, from Aladdin), oleylamine (OAm, 80–90% pure, from Aladdin), 1-octadecene (ODE, >80% pure, from Aladdin), and *n*-octane (>98% pure, from TCI) were used. Toluene, isopropanol and ethyl acetate were of analytical grade and were used as received without further purification. PTAA and TPBi were purchased from Xi'an Polymer Light Technology Corp.

### Synthetic procedures

First, 0.15 M cesium precursor was prepared by loading 2.5 g CsSt and 2 mL OA into 40 mL ODE, and the solution was completely dissolved after heating to 140 °C for 0.5 h. Ten mL of ODE, 1.5 mL of OAm, 2 mL of OA, PbI<sub>2</sub> (0.25 g) and ZnAc (0.045 g)/ZnAcAc (0.07 g)/ZnSt (0.17 g) were loaded into a 100 mL four-neck flask, degassed at 110 °C for 10 min, mixed at 110 °C for 20 min and heated to 180 °C in 10 min under Ar flow. Then, 0.75 mL of CsSt solution (0.15 M in ODE) was quickly injected. After 15 s, the reaction mixture was cooled by the ice-water bath. Then, isopropanol was added into the crude solution with a volume ratio of 2 : 1; the precipitate was collected separately after centrifugation and dispersed in toluene. Ethyl acetate was added into the toluene dispersion; the precipitate was collected and redispersed in *n*-octane.

### Device fabrication

PEDOT:PSS solutions (Baytron P VPAI 4083, filtered through a 0.22 μm filter) were spin-coated onto the ITO-coated glass substrates at 4000 rpm for 60 s and baked at 140 °C for 15 min. The PTAA (in chlorobenzene 5 mg mL<sup>−1</sup>) and CsPbI<sub>3</sub> QDs (in *n*-octane 20 mg mL<sup>−1</sup>) were deposited layer-by-layer by spin coating at 2000 rpm for 60 s. The PTAA and QD layers were baked at 120 °C for 15 min and 60 °C for 10 min, respectively, before the deposition of the next layer. TPBi (40 nm) and LiF/Al electrodes (1 nm/100 nm) were deposited using a thermal evaporation system through a shadow mask under a high vacuum of ~2 × 10<sup>−4</sup> Pa. The device active area was 4 mm<sup>2</sup>, as defined by the overlapping area of the ITO and Al electrodes.

### Characterization and device measurements

One drop of the diluted as-synthesized CsPbI<sub>3</sub> QD dispersion was placed onto a carbon-coated Cu grid, and octane was allowed to evaporate at room temperature. TEM images were taken on a Tecnai G2 F30 S-TWIN TEM instrument operated at an acceleration voltage of 200 kV and equipped with an EDX/STEM HAADF detector. XRD samples were prepared by dropping the purified QD inks onto glass substrates. XRD patterns were acquired using a Bruker D8 Advance X-ray diffractometer operating with Cu Kα radiation (λ = 1.5406 Å). PDF data were achieved by high energy XRD experiments conducted at the beamline 11-ID-C, Advanced Photon Source, Argonne National Laboratory. The wavelength of the X-ray was 0.1173 Å. The diffraction spectra were acquired in transmission geometry by a 2D detector. To evaluate film roughness, QD inks were spin-coated onto Si substrates and then analysed by a Veeco D3100 AFM tool. The absorbance of the QD octane solution was measured by a Shimadzu UV-3600 UV/VIS/NIR spectrophotometer. The PL spectra of the QDs were obtained by using a Varian Cary Eclipse spectrometer. XPS spectra were recorded on a Thermo ESCALAB-250 spectrometer using a monochromatic Al KR radiation source (1486.6 eV). XPS samples were prepared by dropping the purified QD inks onto glasses. The absolute PLQY was measured using a Horiba Fluorolog system equipped with a single grating and a Quanta-Phil integration sphere.

coupled to the Fluorolog system. The PL decay was measured on a time-correlated single-photo counting (TCSPC) spectrofluorometer (FLS920, Edinburg Instrument, U.K.) at room temperature (EPL-455 nm). The EL spectra,  $I$ - $J$ - $V$  characteristics and EQE were collected by using a Keithley 2400 source, a fibre integration sphere, and a PMA-12 spectrometer for light output measurements in a glovebox filled with  $N_2$  at room temperature (the measurement equipment was designed by Hamamatsu Photonics Co., Ltd).

## Conflicts of interest

There are no conflicts to declare.

## Acknowledgements

This work was financially supported by NSFC (51922049, 61604074), the National Key Research and Development Program of China (2016YFB0401701), the Natural Science Foundation of Jiangsu Province (BK20180020), the Fundamental Research Funds for the Central Universities (30917011202), and PAPD of Jiangsu Higher Education Institutions. This research used the resources of the Advanced Photon Source, a US Department of Energy (DOE) Office of Science User Facility operated for the DOE Office of Science by Argonne National Laboratory under Contract No. DE-AC02-06CH11357.

## Notes and references

- 1 X. W. Gong, Z. Y. Yang, G. Walters, R. Comin, Z. J. Ning, E. Beauregard, V. Adinolfi, O. Voznyy and E. H. Sargent, Highly efficient quantum dot near-infrared light-emitting diodes, *Nat. Photonics*, 2016, **10**, 253–257.
- 2 Z. K. Tan, R. S. Moghaddam, M. L. Lai, P. Docampo, R. Higler, F. Deschler, M. Price, A. Sadhanala, L. M. Pazos, D. Credgington, F. Hanusch, T. Bein, H. J. Snaith and R. H. Friend, Bright light-emitting diodes based on organometal halide perovskite, *Nat. Nanotechnol.*, 2014, **9**, 687–692.
- 3 Q. A. Akkerman, G. Raino, M. V. Kovalenko and L. Manna, Genesis, challenges and opportunities for colloidal lead halide perovskite nanocrystals, *Nat. Mater.*, 2018, **17**, 394–405.
- 4 J. H. Li, L. M. Xu, T. Wang, J. Z. Song, J. W. Chen, J. Xue, Y. H. Dong, B. Cai, Q. S. Shan, B. N. Han and H. B. Zeng, 50-fold EQE improvement up to 6.27% of solution-processed all-inorganic perovskite  $CsPbBr_3$  QLEDs via surface ligand density control, *Adv. Mater.*, 2017, **29**, 1703885.
- 5 S. Yuan, Z. K. Wang, L. X. Xiao, C. F. Zhang, S. Y. Yang, B. B. Chen, H. T. Ge, Q. S. Tian, Y. Jin and L. S. Liao, Optimization of low-dimensional components of quasi-2D perovskite films for deep-blue light-emitting diodes, *Adv. Mater.*, 2019, **31**, 1904319.
- 6 J. Z. Song, J. H. Li, L. M. Xu, J. H. Li, F. J. Zhang, B. N. Han, Q. S. Shan and H. B. Zeng, Room-temperature triple-ligand surface engineering synergistically boosts ink stability, recombination dynamics, and charge injection toward EQE-11.6% perovskite QLEDs, *Adv. Mater.*, 2018, **30**, 1800764.
- 7 J. Z. Song, T. Fang, J. H. Li, L. M. Xu, F. J. Zhang, B. N. Han, Q. S. Shan and H. B. Zeng, Organic-inorganic hybrid passivation enables perovskite QLEDs with an EQE of 16.48%, *Adv. Mater.*, 2018, **30**, 1805409.
- 8 T. Chiba, Y. Hayashi, H. Ebe, K. Hoshi, J. Sato, S. Sato, Y. J. Pu, S. Ohisa and J. Kido, Anion-exchange red perovskite quantum dots with ammonium iodine salts for highly efficient light-emitting devices, *Nat. Photonics*, 2018, **12**, 681–689.
- 9 S. Hou, M. K. Gangishetty, Q. Quan and D. N. Congreve, Efficient blue and white perovskite light-emitting diodes via manganese doping, *Joule*, 2018, **2**, 2421–2433.
- 10 J. Z. Song, J. H. Li, X. M. Li, L. M. Xu, Y. H. Dong and H. B. Zeng, Quantum dot light-emitting diodes based on inorganic perovskite cesium lead halides ( $CsPbX_3$ ), *Adv. Mater.*, 2015, **27**, 7162–7167.
- 11 M. Lu, X. Zhang, X. Bai, H. Wu, X. Shen, Y. Zhang, W. Zhang, W. Zheng, H. Song, W. W. Yu and A. L. Rogach, Spontaneous silver doping and surface passivation of  $CsPbI_3$  perovskite active layer enable light-emitting devices with an external quantum efficiency of 11.2%, *ACS Energy Lett.*, 2018, **3**, 1571–1577.
- 12 J. C. Yu, D. B. Kim, E. D. Jung, B. R. Lee and M. H. Song, High-performance perovskite light-emitting diodes via morphological control of perovskite films, *Nanoscale*, 2016, **8**, 7036–7042.
- 13 S. J. Lee, J. H. Park, B. R. Lee, E. D. Jung, J. C. Yu, D. Di Nuzzo, R. H. Friend and M. H. Song, Amine-based passivating materials for enhanced optical properties and performance of organic inorganic perovskites in light-emitting diodes, *J. Phys. Chem. Lett.*, 2017, **8**, 1784–1792.
- 14 D. W. deQuilettes, S. Koch, S. Burke, R. K. Paranj, A. J. Shropshire, M. E. Ziffer and D. S. Ginger, Photoluminescence lifetimes exceeding 8  $\mu$ s and quantum yields exceeding 30% in hybrid perovskite thin films by ligand passivation, *ACS Energy Lett.*, 2016, **1**, 438–444.
- 15 J. Byun, H. Cho, C. Wolf, M. Jang, A. Sadhanala, R. H. Friend, H. Yang and T. W. Lee, Efficient visible quasi-2D perovskite light-emitting diodes, *Adv. Mater.*, 2016, **28**, 7515–7520.
- 16 S. Lee, D. B. Kim, J. C. Yu, C. H. Jang, J. H. Park, B. R. Lee and M. H. Song, Versatile defect passivation methods for metal halide perovskite materials and their application to light-emitting devices, *Adv. Mater.*, 2019, **31**, 1805244.
- 17 J. Q. Li, S. G. R. Bade, X. Shan and Z. B. Yu, Single-layer light-emitting diodes using organometal halide perovskite/poly(ethylene oxide) composite thin films, *Adv. Mater.*, 2015, **27**, 5196–5202.
- 18 M. J. Yuan, L. N. Quan, R. Comin, G. Walters, R. Sabatini, O. Voznyy, S. Hoogland, Y. B. Zhao, E. M. Beauregard, P. Kanjanaboos, Z. H. Lu, D. H. Kim and E. H. Sargent, Perovskite energy funnels for efficient light-emitting diodes, *Nat. Nanotechnol.*, 2016, **11**, 872–879.
- 19 Y. H. Kim, J. S. Kim and T. W. Lee, Strategies to improve luminescence efficiency of metal-halide perovskites and light-emitting diodes, *Adv. Mater.*, 2018, **31**, 1804595.
- 20 T. Fang, F. Zhang, S. Yuan, H. Zeng and J. Song, Recent advances and prospects toward blue perovskite materials and light-emitting diodes, *InfoMat*, 2019, **1**, 211.

- 21 C. H. A. Li, Z. Zhou, P. Vashishtha and J. E. Halpert, The future is blue (LEDs): why chemistry is the key to perovskite displays, *Chem. Mater.*, 2019, **31**, 6003–6032.
- 22 T. Wang, V. Chirmanov, W. H. M. Chiu and P. V. Radovanovic, Generating tunable white light by resonance energy transfer in transparent dye-conjugated metal oxide nanocrystals, *J. Am. Chem. Soc.*, 2013, **135**, 14520–14523.
- 23 A. Nag and D. D. Sarma, White light from Mn<sup>2+</sup>-doped CdS nanocrystals: a new approach, *J. Phys. Chem. C*, 2007, **111**, 13641–13644.
- 24 J. W. Stouwdam and R. A. J. Janssen, Electroluminescent Cu-doped CdS quantum dots, *Adv. Mater.*, 2009, **21**, 2916–2920.
- 25 P. K. Santra and P. V. Kamat, Mn-doped quantum dot sensitized solar cells: a strategy to boost efficiency over 5%, *J. Am. Chem. Soc.*, 2012, **134**, 2508–2511.
- 26 Z. Yang, J. Song, H. Zeng and M. Wang, Organic composition tailored perovskite solar cells and light-emitting diodes: perspectives and advances, *Mater. Today Energy*, 2019, **14**, 100338.
- 27 A. K. Jena, A. Kulkarni, Y. Sanehira, M. Ikegami and T. Miyasaka, Stabilization of  $\alpha$ -CsPbI<sub>3</sub> in ambient room temperature conditions by incorporating Eu into CsPbI<sub>3</sub>, *Chem. Mater.*, 2018, **30**, 6668–6674.
- 28 L. Xu, S. Yuan, H. Zeng and J. Song, A comprehensive review of doping in perovskite nanocrystals/quantum dots: evolution of structure, electronics, optics, and light-emitting diodes, *Mater. Today Nano*, 2019, **6**, 100036.
- 29 K. Xu, A. C. Allen, B. B. Luo, E. T. Vickers, Q. H. Wang, W. R. Hollingsworth, A. L. Ayzner, X. M. Li and J. Z. Zhang, Tuning from quantum dots to magic sized clusters of CsPbBr<sub>3</sub> using novel planar ligands based on the trivalent nitrate coordination complex, *J. Phys. Chem. Lett.*, 2019, **10**, 4409–4416.
- 30 J. Cao, S. X. Tao, P. A. Bobbert, C. P. Wong and N. Zhao, Interstitial occupancy by extrinsic alkali cations in perovskites and its impact on ion migration, *Adv. Mater.*, 2018, **30**, 1707350.
- 31 M. Lu, X. Y. Zhang, Y. Zhang, J. Guo, X. Y. Shen, W. W. Yu and A. L. Rogach, Simultaneous strontium doping and chlorine surface passivation improve luminescence intensity and stability of CsPbI<sub>3</sub> nanocrystals enabling efficient light-emitting devices, *Adv. Mater.*, 2018, **30**, 1804691.
- 32 X. Y. Shen, Y. Zhang, S. V. Kershaw, T. S. Li, C. C. Wang, X. Y. Zhang, W. Y. Wang, D. G. Li, Y. H. Wang, M. Lu, L. J. Zhang, C. Sun, D. Zhao, G. S. Qin, X. Bai, W. W. Yu and A. L. Rogach, Zn-alloyed CsPbI<sub>3</sub> nanocrystals for highly efficient perovskite light-emitting devices, *Nano Lett.*, 2019, **19**, 1552–1559.
- 33 W. Zhao, D. Yang, Z. Yang and S. Liu, Zn-doping for reduced hysteresis and improved performance of methylammonium lead iodide perovskite hybrid solar cells, *Mater. Today Energy*, 2017, **5**, 205–213.
- 34 U. Khan, Z. N. Yu, A. A. Khan, A. Zulfiqar and N. Ullah, High-Performance CsPbI<sub>2</sub>Br perovskite solar cells with zinc and manganese doping, *Nanoscale Res. Lett.*, 2019, **14**, 11671.
- 35 W. van der Stam, J. J. Geuchies, T. Altantzis, K. H. W. van den Bos, J. D. Meeldijk, S. Van Aert, S. Bals, D. Vanmaekelbergh and C. de Mello Donega, Highly emissive divalent-ion-doped colloidal CsPb<sub>1-x</sub>M<sub>x</sub>Br<sub>3</sub> perovskite nanocrystals through cation exchange, *J. Am. Chem. Soc.*, 2017, **139**, 4087–4097.
- 36 M. I. Saidaminov, J. Kim, A. Jain, R. Quintero-Bermudez, H. R. Tan, G. K. Long, F. R. Tan, A. Johnston, Y. C. Zhao, O. Voznyy and E. H. Sargent, Suppression of atomic vacancies *via* incorporation of isovalent small ions to increase the stability of halide perovskite solar cells in ambient air, *Nat. Energy*, 2018, **3**, 648–654.
- 37 A. Swarnkar, W. J. Mir and A. Nag, Can B-site doping or alloying improve thermal- and phase-stability of all-inorganic CsPbX<sub>3</sub> (X = Cl, Br, I) perovskites?, *ACS Energy Lett.*, 2018, **3**, 286–289.
- 38 Y. T. Dong, T. Qiao, D. Kim, D. Parobek, D. Rossi and D. H. Son, Precise control of quantum confinement in cesium lead halide perovskite quantum dots via thermodynamic equilibrium, *Nano Lett.*, 2018, **18**, 3716–3722.
- 39 Y. H. Kye, C. J. Yu, U. G. Jong, K. C. Ri, J. S. Kim, S.-H. Choe, S.-N. Hong, S. Li, J. N. Wilson and A. Walsh, Vacancy-driven stabilization of the cubic perovskite polymorph of CsPbI<sub>3</sub>, *J. Phys. Chem. C*, 2019, **123**, 9735–9744.
- 40 P. Z. Liu, W. Chen, W. G. Wang, B. Xu, D. Wu, J. J. Hao, W. Y. Cao, F. Fang, Y. Li, Y. Y. Zeng, R. K. Pan, S. M. Chen, W. Q. Cao, X. W. Sun and K. Wane, Halide-rich synthesized cesium lead bromide perovskite nanocrystals for light-emitting diodes with improved performance, *Chem. Mater.*, 2017, **29**, 5168–5173.
- 41 Q. Lin, B. Song, H. Wang, F. Zhang, F. Chen, L. Wang, L. S. Li, F. Guo and H. Shen, High-efficiency deep-red quantum-dot light-emitting diodes with type-II CdSe/CdTe core/shell quantum dots as emissive layers, *J. Mater. Chem. C*, 2016, **4**, 7223–7229.
- 42 B. Jeong, H. Han, Y. J. Choi, S. H. Cho, E. H. Kim, S. W. Lee, J. S. Kim, C. Park, D. Kim and C. Park, All-inorganic CsPbI<sub>3</sub> perovskite phase-stabilized by poly(ethylene oxide) for red-light-emitting diodes, *Adv. Funct. Mater.*, 2018, **28**, 1706401.
- 43 J. Berry, T. Buonassisi, D. A. Egger, G. Hodes, L. Kronik, Y. L. Loo, I. Lubomirsky, S. R. Marder, Y. Mastai, J. S. Miller, D. B. Mitzi, Y. Paz, A. M. Rappe, I. Riess, B. Rybtchinski, O. Stafsudd, V. Stevanovic, M. F. Toney, D. Zitoun, A. Kahn, D. Ginley and D. Cahen, Hybrid organic–inorganic perovskites (HOIPs): opportunities and challenges, *Adv. Mater.*, 2015, **27**, 5102–5112.
- 44 L. L. Meng, L. F. Liang and Y. X. Wen, Deep red phosphors SrMgAl<sub>10</sub>O<sub>17</sub>:Mn<sup>4+</sup>, M (M = Li<sup>+</sup>, Na<sup>+</sup>, K<sup>+</sup>, Cl<sup>−</sup>) for warm white light emitting diodes, *J. Mater. Sci.: Mater. Electron.*, 2014, **25**, 2676–2681.
- 45 J. F. Yuan, C. H. Bi, S. X. Wang, R. Q. Guo, T. Shen, L. X. Zhang and J. J. Tian, Spray-coated colloidal perovskite quantum dot films for highly efficient solar cells, *Adv. Funct. Mater.*, 2019, **29**, 1906615.
- 46 C. H. Bi, S. V. Kershaw, A. L. Rogach and J. J. Tian, Improved stability and photodetector performance of CsPbI<sub>3</sub> perovskite quantum dots by ligand exchange with aminoethanethiol, *Adv. Funct. Mater.*, 2019, **29**, 1902446.
- 47 L. Protesescu, S. Yakunin, M. I. Bodnarchuk, F. Krieg, R. Caputo, C. H. Hendon, R. X. Yang, A. Walsh and M. V. Kovalenko,

- Nanocrystals of cesium lead halide perovskites ( $\text{CsPbX}_3$ ,  $\text{X} = \text{Cl}$ ,  $\text{Br}$ , and  $\text{I}$ ): novel optoelectronic materials showing bright emission with wide color gamut, *Nano Lett.*, 2015, **15**, 3692–3696.
- 48 A. Swarnkar, A. R. Marshall, E. M. Sanehira, B. D. Chernomordik, D. T. Moore, J. A. Christians, T. Chakrabarti and J. M. Luther, Quantum dot-induced phase stabilization of  $\alpha\text{-CsPbI}_3$  perovskite for high-efficiency photovoltaics, *Science*, 2016, **354**, 92–95.
  - 49 Z. Li, M. J. Yang, J. S. Park, S. H. Wei, J. J. Berry and K. Zhu, Stabilizing perovskite structures by tuning tolerance factor: formation of formamidinium and cesium lead iodide solid-state alloys, *Chem. Mater.*, 2016, **28**, 284–292.
  - 50 R. E. Eitel, C. A. Randall, T. R. Shrout, P. W. Rehrig, W. Hackenberger and S. E. Park, New high temperature morphotropic phase boundary piezoelectrics based on  $\text{Bi}(\text{Me})\text{O}_3\text{-PbTiO}_3$  ceramics, *Jpn. J. Appl. Phys.*, 2001, **40**, 5999–6002.
  - 51 W. H. Ning, X. G. Zhao, J. Klarbring, S. Bai, F. X. Ji, F. Wang, S. I. Simak, Y. T. Tao, X. M. Ren, L. J. Zhang, W. Huang, I. A. Abrikosov and F. Gao, Thermochromic lead-free halide double perovskites, *Adv. Funct. Mater.*, 2019, **29**, 1807375.
  - 52 S. Sanchez, U. Steiner and X. Hua, Phase evolution during perovskite formation-insight from pair distribution function analysis, *Chem. Mater.*, 2019, **31**, 3498–3506.
  - 53 S. J. Ikhmayies and R. N. Ahmad-Bitar, An investigation of the bandgap and Urbach tail of vacuum-evaporated  $\text{SnO}_2$  thin films, *Renewable Energy*, 2013, **49**, 143–146.
  - 54 T. A. Wassner, B. Laumer, S. Maier, A. Laufer, B. K. Meyer, M. Stutzmann and M. Eickhoff, Optical properties and structural characteristics of  $\text{ZnMgO}$  grown by plasma assisted molecular beam epitaxy, *J. Appl. Phys.*, 2009, **105**, 023505.
  - 55 Z. Tang, S. Tanaka, S. Ito, S. Ikeda, K. Taguchi and T. Minemoto, Investigating relation of photovoltaic factors with properties of perovskite films based on various solvents, *Nano Energy*, 2016, **21**, 51–61.
  - 56 D. Shi, V. Adinolfi, R. Comin, M. J. Yuan, E. Alarousu, A. Buin, Y. Chen, S. Hoogland, A. Rothenberger, K. Katsiev, Y. Losovyj, X. Zhang, P. A. Dowben, O. F. Mohammed, E. H. Sargent and O. M. Bakr, Low trap-state density and long carrier diffusion in organolead trihalide perovskite single crystals, *Science*, 2015, **347**, 519–522.
  - 57 H. C. Zai, C. Zhu, H. P. Xie, Y. Z. Zhao, C. B. Shi, Z. X. Chen, X. X. Ke, M. L. Sui, C. F. Chen, J. S. Hu, Q. S. Zhang, Y. L. Gao, H. P. Zhou, Y. J. Li and Q. Chen, Congeneric incorporation of  $\text{CsPbBr}_3$  nanocrystals in a hybrid perovskite heterojunction for photovoltaic efficiency enhancement, *ACS Energy Lett.*, 2018, **3**, 30–38.